



Cite this: DOI: 10.1039/d5mh01846c

Received 27th September 2025,
Accepted 18th November 2025

DOI: 10.1039/d5mh01846c

rsc.li/materials-horizons

Electromagnetic interference (EMI) presents a critical challenge across application areas such as wireless communication networks, defense technologies, and electronic devices. Although metamaterial absorbers offer excellent electromagnetic (EM) wave attenuation, their limited mechanical stiffness restricts their use in structurally demanding environments. This study introduces a new class of layered hybrid lattice absorbers that concurrently achieve broadband EM wave absorption and enhanced mechanical stiffness. Three-layer hybrid lattices are developed by combining simple cubic (SC), body-centered cubic (BC), and octet-truss (OT) architectures in diverse configurations. The relationship between broadband absorption and mechanical performance is then examined as a function of lattice arrangement. Finite element simulations are used to evaluate EM responses and effective stiffness across the 4–18 GHz frequency range. The simulations show that positioning an OT lattice in the upper layer leads to average EM absorption exceeding 95% due to improved impedance matching, whereas the middle layer primarily regulates how the residual energy is redistributed within the multilayer system. Incorporating an SC lattice in the lower layer enhances the structure's load-bearing capacity. We find that the OT–SC–SC configuration maintains strong EM absorption while providing approximately 36% greater stiffness in the out-of-plane (vertical stacking) direction and 118% greater stiffness in the in-plane directions relative to the benchmark OT–OT–OT configuration. These findings highlight that tailored spatial arrangement of lattice types enables simultaneous optimization of EM and mechanical functionalities. Positioning an OT lattice at the top and an SC lattice at the bottom is demonstrated to be an effective strategy for developing multifunctional metamaterial absorbers. This approach offers a foundational framework for next-generation absorbers targeting advanced EMI shielding and mechanically resilient applications.

Layered hybrid lattice architectures for broadband electromagnetic absorption and improved structural stiffness

Hyoui Yoon, ^{ab} Dahyun Daniel Lim, ^{cd} Grace X. Gu, ^d and Sangryun Lee, ^{*ab}

New concepts

This study introduces a new design paradigm for multifunctional metamaterials through layered hybrid lattice absorbers that achieve a balance between broadband electromagnetic absorption and mechanical stiffness. Unlike lattice-based metamaterial studies that typically focused on either electromagnetic absorption or mechanical stiffness in isolation, the present work explores how the stacking order of different lattice types governs both physical characteristics. While previous studies mainly relied on modifying geometric parameters within a single lattice type, this work employs the spatial arrangement of distinct lattice architectures as an active design variable to realize complementary electromagnetic and mechanical functions. Results show that the octet-truss top layer improves impedance matching and enhances absorption efficiency, whereas a simple cubic bottom layer reinforces load-bearing capacity and overall stiffness. This finding establishes a framework for balancing competing performance metrics within a single system, providing a pathway toward tunable, performance-balanced metamaterials that are well suited for lightweight, mechanically robust, and broadband electromagnetic interference (EMI) shielding applications.

1. Introduction

Advancements in electromagnetic (EM)-wave-based technologies have facilitated the development of modern systems such as wireless communications, devices, and 5G networks, thereby improving daily life and boosting industrial productivity.^{1–4} However, these advancements have also intensified EM interference (EMI), which undermines device performance and raises safety concerns, particularly in aviation and defense applications.^{5–7} Likewise, the increasing deployment of domain controllers in industrial environments has aggravated EMI issues, reinforcing the need for effective EM wave absorption strategies.⁸ Consequently, EM wave absorbers (EMAs) have

^a Department of Mechanical and Biomedical Engineering, Ewha Womans University, Seoul 03760, Republic of Korea. E-mail: sr.lee@ewha.ac.kr

^b Graduate Program in System Health Science and Engineering, Ewha Womans University, Seoul 03760, Republic of Korea

^c School of Mechanical Engineering, Korea University, Seoul, 02841, Republic of Korea

^d Department of Mechanical Engineering, University of California, Berkeley, CA 94720, USA

become essential for supporting EM safety and environmental stability.⁹ Accordingly, the development of high-performance EMAs has emerged as a central research priority across diverse sectors.

Although metal-, carbon-, and ferrite-based EMAs have been studied extensively, most still exhibit inadequate dielectric permittivity or magnetic permeability for broadband absorption.^{10,11} Moreover, conventional EMAs with planar configurations are bulky and heavy, which limits their applicability in broadband systems.^{12,13} To overcome these shortcomings, carbon-based materials, such as carbon nanotubes and graphite, have been proposed as lightweight, highly conductive alternatives to metal-based EMAs; however, their thermal stability warrants further improvement.^{14,15} While these materials maintain relatively stable absorption over broad frequency ranges, their peak efficiency remains limited in certain bands owing to residual impedance mismatch arising primarily from dielectric loss.^{16–18} Their environmental durability also remains inadequate for practical deployment.¹⁹ In contrast, ferrite-based absorbers rely on magnetic loss to achieve strong absorption in the low-frequency range (*e.g.*, 1.8–5.5 GHz for various doped spinel ferrites).²⁰ Nevertheless, their high density and weight,²¹ coupled with a steep decline in absorption efficiency above 8 GHz, restrict their suitability for high-frequency EMI mitigation.²²

To address these limitations in absorption bandwidth, weight, and durability, researchers have introduced meta-material absorbers.²³ Unlike traditional materials that rely on intrinsic material properties, metamaterials harness structural and geometric design to absorb EM waves, enabling compact profiles and high absorption efficiency at specific frequencies. While geometry-based control of wave propagation is also explored in other physical domains such as acoustic or phononic systems, EM metamaterials uniquely exploit structural design to achieve impedance matching and power dissipation across broad frequency ranges. For instance, Lim *et al.*²⁴ analyzed how several structural parameters of lattice architectures influence absorption efficiency and underlying mechanisms. Specifically, they demonstrated that variations in unit-cell geometry, including strut thickness, lattice constant, and volume fraction, directly affect impedance matching and energy dissipation behavior. Their results revealed that thinner struts and smaller lattice constants enhance high-frequency absorption by increasing multiple internal reflections and power loss within the lattice network. These engineered structures also offer flexible architectures that grant control over effective complex permeability and permittivity, thereby exceeding the performance limits of conventional materials.²⁵

With recent advances in fabrication techniques, the design and development of geometrically complex broadband meta-material absorbers have also become feasible.^{26,27} Building upon these manufacturing innovations, Lim *et al.*²⁶ built multilayer lattice structures composed of a single type of unit cell, demonstrating that layer stacking can effectively enhance broadband absorption performance. Similarly, Zhou *et al.*²⁷ reported that multilayer configurations formed from small

periodic lattices induce multiple internal reflections and interference, thereby improving overall absorption efficiency. According to these previous studies, as the unit cell size decreases, the structures behave as effective medium and promote impedance matching.^{24,27} Consequently, multilayer designs yield lower reflection loss than their single-layer counterparts of equivalent thickness and deliver superior absorption across the 8–40 GHz range.⁵ However, most existing lattice-structured absorbers have been designed focusing on EM wave absorption, often overlooking mechanical stiffness requirements,^{26,28} but given the inherently high porosity of lattice architectures, evaluating their effective stiffness becomes critical.²⁹ If the stiffness is inadequate, structural deformation may occur under external impact or vibration, which can, in turn, compromise EM wave absorption performance.^{30–32}

To address the trade-off between EM wave absorption and mechanical stiffness, this study introduces a three-layer hybrid lattice structure that combines high EM absorption efficiency with mechanical rigidity. In contrast to earlier studies that optimized only geometric parameters of a single lattice type, this work utilizes the spatial organization of distinct lattice architectures as a key design variable, enabling complementary enhancement of electromagnetic absorption and mechanical stiffness. Specifically, our design incorporates simple cubic (SC), body-centered cubic (BC), and octet-truss (OT) lattices, and their EM absorption and mechanical behavior is evaluated through computational modeling and simulation. EM performance is further assessed using finite element analysis (FEA), which resolves frequency-dependent power loss and scattering parameters. The EM response is analyzed across the C-band (4–8 GHz), X-band (8–12 GHz), and Ku-band (12–18 GHz), which are frequency ranges relevant to various applications.³³ Mechanical stiffness and structural integrity are characterized using homogenization theory, which quantifies stress distributions and relative stiffness under defined load conditions. Overall, this study establishes a design methodology that overcomes the stiffness limitations of conventional multilayer absorbers while preserving reliable EM absorption performance.

2. Materials and methods

A hybrid lattice composed of SC, BC, and OT unit cells is modeled using the experimentally measured material properties of carbon black–polylactic acid (CB–PLA), whose dielectric loss characteristics provide strong EM wave attenuation and whose printability is experimentally validated through fused filament fabrication (FFF) in previous research.^{24,26} In particular, multilayer OT lattice absorbers with a 10 mm unit-cell length and 1.2 mm strut diameter were successfully fabricated using a standard 0.4 mm FFF nozzle without structural defects. This confirms the feasibility of realizing geometrically complex polymer lattice architectures through conventional additive manufacturing techniques. The hybrid design proposed in this

study aims to enhance both EM wave absorption and mechanical stiffness by leveraging the complementary advantages of each unit cell geometry.

2.1. Unit cell geometry design

To evaluate the EM and mechanical characteristics of the constituent lattice structures, three distinct unit cell configurations—SC, BC, and OT—are modeled in COMSOL Multiphysics.³⁴ Each structure is designed with a total thickness of 30 mm and is categorized as either a single-layer or multi-layer configuration. In single-layer designs, a single 30 mm unit cell is used (a_1), while multi-layer designs consist of three stacked 10 mm unit cells (a_2), as illustrated in Fig. 1(a). To maintain a consistent volume fraction across all lattices, the strut radii are adjusted accordingly. Fig. 1(b) presents the stacking arrangements used for the different lattices. In multi-layer designs, different lattice types are combined across layers. This stacking strategy supports broadband EM wave absorption and enhances structural stability by integrating the EM and mechanical properties of the constituent layers.

2.2. EM simulations

Three-dimensional EM simulations are conducted using the RF Module in COMSOL Multiphysics to evaluate the EM response of the designed lattice structures (Fig. 2(a)). Although the lattice constant ($a_2 = 10$ mm) is comparable to the shortest wavelength ($\lambda = 16.7$ mm at 18 GHz), the struts forming each unit cell (~ 0.3 mm) remain sufficiently smaller than λ , maintaining a subwavelength scale, ($\approx \lambda/50$).²⁴ These simulations yield electric field (E-field) and magnetic field (M-field) distributions, power loss, and scattering parameters (S-parameters). Fig. 2(b) depicts the E-field distribution at 14 GHz. These outputs are used to determine the reflection, transmission, and absorption characteristics of each structure. Floquet-periodic boundary conditions are applied to all lateral surfaces to replicate periodic lattice arrays. The lattice material is defined as CB-PLA, and the surrounding medium is set to air. The frequency-dependent permittivity values of CB-PLA used in the simulations are listed in Table 1.²⁴ Two ports are positioned on the top and bottom surfaces to record S-parameters, with the EM waves propagating in the negative z -direction. Perfectly matched

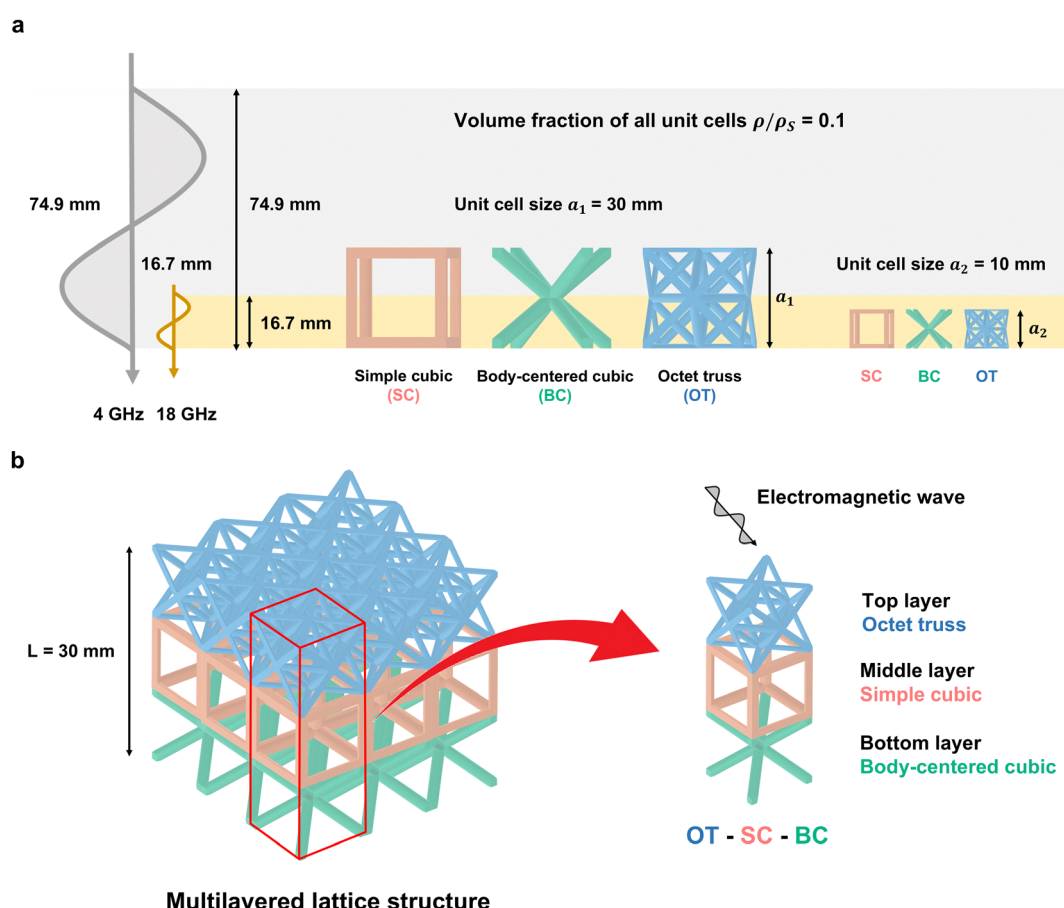


Fig. 1 (a) Schematic comparison of EM wavelengths at 4 GHz ($\lambda = 74.9$ mm) and 18 GHz ($\lambda = 16.7$ mm), along with the unit cell sizes used in this study: $a_1 = 30$ mm for single-layer structures and $a_2 = 10$ mm for multilayer lattices. These dimensions are selected to ensure a constant total thickness of 30 mm. (b) Conceptual diagram of the multilayer lattice absorber, comprising three vertically stacked lattice layers with a uniform lattice constant of 10 mm. From bottom to top, BC, SC, and OT unit cells are assigned. EM waves are incident from the top (OT layer).

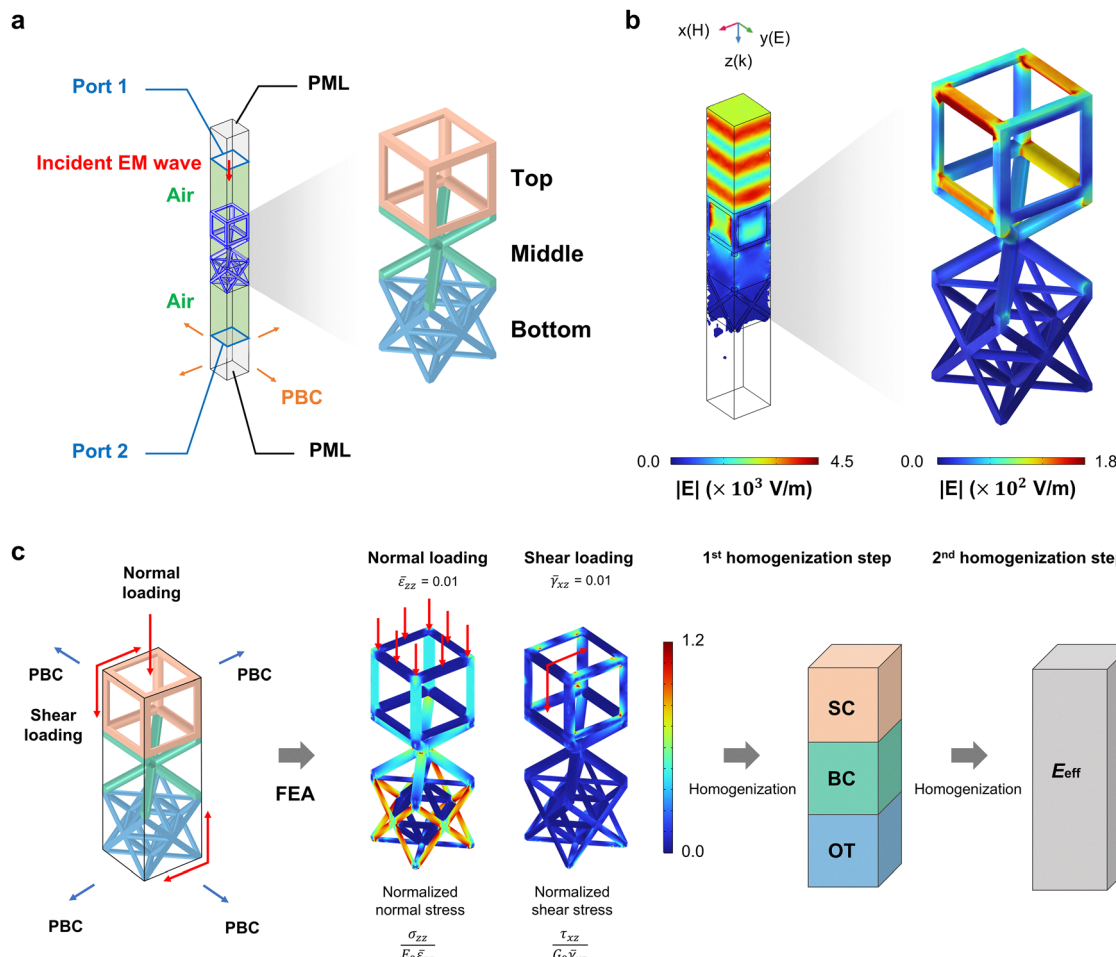


Fig. 2 (a) Simulation setup for analyzing EM wave absorption in multilayer lattice structures. An EM wave is incident along the z -direction from Port 1, with Floquet-periodic boundary conditions applied to the lateral surfaces to model an infinite array. Air domains are added above and below the lattice. (b) Electric field distribution at 14 GHz. (c) Simulation setup and schematic of the two-step homogenization workflow used to evaluate the effective modulus of each three-layer lattice. Periodic boundary conditions are applied to all side surfaces, and a 1% compressive strain is imposed along the z -direction at the top surface. The color maps depict the normalized stress distribution under 1% compressive and shear strain loading.

Table 1 EM properties of CB-PLA and air used in the EM simulations. f denotes frequency (GHz)

Property	CB-PLA	Air Unit
Electrical conductivity	0	0 S m^{-1}
Relative permeability	1	1
Real permittivity (ϵ')	$(f - 8.2) \times (-0.9457) + 17.73$	1
Imaginary permittivity (ϵ'')	$(f - 8.2) \times (-1.40704) + 24.7101$	0
Relative permittivity (ϵ)	$\epsilon' - j\epsilon''$	1

layers are applied to the top and bottom boundaries to absorb outgoing waves and suppress edge reflections.

The incident wave frequency spans 4–18 GHz, covering the C-band (4–8 GHz), X-band (8–12 GHz), and Ku-band (12–18 GHz). Quadratic tetrahedral elements are employed to generate the mesh, with the element size kept below 5% of the incident wavelength to ensure both accuracy and convergence. The mesh is refined separately for the air and solid domains: The air domain contains more than 164 000 elements with a

maximum size of approximately 0.1 mm, whereas the solid domain comprises over 27 000 elements with element sizes smaller than 0.03 mm to resolve the lattice struts, as illustrated in Fig. S1. As shown in Fig. S1, a mesh convergence test is performed by varying the maximum element sizes of the air and solid domains. The results confirm that the difference in absorption across the 4–18 GHz range remained within 0.1% compared with the finest mesh, verifying that the mesh size used in this study provides sufficient numerical accuracy and reliability. The EM response is evaluated by calculating reflection (R), transmission (T), and absorption (A) from the simulated S -parameters. Reflection is derived from the reflection coefficient S_{11} , as detailed in eqn (1).

$$R = |S_{11}|^2 \quad (1)$$

Transmission is obtained from the transmission coefficient S_{21} , as presented in eqn (2).

$$T = |S_{21}|^2 \quad (2)$$

Absorption, representing the fraction of incident EM energy absorbed by the structure, is computed using eqn (3).

$$A = 1 - R - T \quad (3)$$

These formulations enable a frequency-dependent analysis of EM absorption for each lattice configuration.

2.3. Effective modulus of the hybrid lattice structures

The mechanical stiffness of the hybrid lattices is evaluated by combining FEA with a two-step homogenization method to calculate the relative modulus. The FEA module in COMSOL Multiphysics incorporates CB-PLA properties (Young's modulus $E_0 = 2.1$ GPa and Poisson's ratio $\nu = 0.35$)³⁵ and applies tie boundary conditions at the interfaces between stacked lattice layers to simulate realistic bonding. A linear-elastic material model is adopted under the assumption of infinitesimal deformation, where the structural response is governed by the scale-free equilibrium relation. Therefore, the effective stiffness depends solely on the relative density and topology.³⁶ In the first homogenization step, the effective stiffness of the unit cell is determined under periodic boundary conditions. Three normal strains ($\varepsilon_{xx}, \varepsilon_{yy}, \varepsilon_{zz} = -0.01$) and three shear strains ($\gamma_{xy}, \gamma_{yz}, \gamma_{xz} = -0.01$) are applied to capture all independent deformation modes. Fig. 2(c) illustrates the FEA setup used to evaluate effective stiffness under representative normal and shear loading conditions. Periodic boundary conditions are imposed on all side faces to ensure displacement compatibility between opposing surfaces and maintain periodicity. During compression, the top surface undergoes displacement-controlled loading in the z -direction ($\varepsilon_{zz} = -0.01$), while the bottom surface remains fixed. Fig. 2(c) also displays normalized stress distributions under compression and xz -shear, enabling a quantitative comparison of relative stress across the lattice layers. These results support the evaluation of layer-specific load-bearing behavior and relative stiffness in the multi-layer configurations.

Stress data from the simulations yield the volume-averaged stress $\bar{\sigma}_{ij}^{(1)}$ within the lattice domain. Eqn (4) applies the homogenization method using the volume fractions c_i of the two phases in the unit lattice cell (0: void, 1: solid phase of the lattice structure):

$$\bar{\sigma}_{ij} = c_0 \bar{\sigma}_{ij}^{(0)} + c_1 \bar{\sigma}_{ij}^{(1)}. \quad (4)$$

Because the matrix is void and the reinforcement corresponds to the lattice structure, the volume-averaged stress in the void phase $\bar{\sigma}_{ij}^{(0)}$ is zero. Thus, the effective stress $\bar{\sigma}_{ij}$ simplifies to the following:

$$\bar{\sigma}_{ij} = c_1 \bar{\sigma}_{ij}^{(1)} = \bar{\rho} \bar{\sigma}_{ij}^{(1)} \quad (5)$$

In the above equation, $\bar{\rho} = \rho/\rho_s$ denotes the relative density of the unit lattice structure, with ρ representing the mass density of the lattice structure and ρ_s signifying the density of the fully dense solid material. Hill's lemma states that the imposed boundary conditions yield an average strain determined by the applied displacement.³⁷ For instance, applying a displacement

$u_z = -0.01a$ to the top surface under normal loading produces an average strain of $\bar{\varepsilon}_{zz} = -0.01$ and the corresponding volume-averaged stress. The relationship between the volume-averaged stress and strain is expressed as

$$\bar{\sigma}_{ij} = C_{ijkl} \bar{\varepsilon}_{kl}. \quad (6)$$

Here, C_{ijkl} denotes the effective stiffness tensor of the lattice structure. The repeated indices k and l follow the Einstein summation convention, indicating summation over the range from one to three. The compliance tensor S_{ijkl} , defined as the inverse of the stiffness tensor, satisfies

$$S_{ijkl} = (C_{ijkl})^{-1}. \quad (7)$$

Sampling over a unit sphere yields the three-dimensional distribution of modulus, $E(n)$. Directional vectors $n(\varphi, \theta) = [\sin \theta \cos \varphi, \sin \theta \sin \varphi, \cos \theta]^T$ span the sphere, where $\varphi \in [0, 2\pi]$ denotes the azimuth angle, and $\theta \in [0, \pi]$ represents the elevation angle. For each direction $n(\varphi, \theta)$, the directional compliance $S(n)$ is calculated as

$$S(n) = n_i n_j n_k n_l S_{ijkl}. \quad (8)$$

The corresponding directional Young's modulus $E(n)$ is obtained as the inverse of the compliance:

$$E(n) = [S(n)]^{-1} = [n_i n_j n_k n_l S_{ijkl}]^{-1}. \quad (9)$$

The directional modulus along the z -axis, E_z , equals S_{3333}^{-1} under a uniaxial strain $\varepsilon_{zz} = -0.01$. Shear moduli G_{xz} , G_{yz} , and G_{xy} are derived by applying shear strains $\gamma = 0.01$ in the xz , yz , and xy planes, respectively. The resulting shear stresses τ_{ij} yield the moduli through the relation $G_{ij} = \tau_{ij}/\gamma_{ij}$, corresponding to stiffness components C_{1313} , C_{2323} , and C_{1212} .

For the second homogenization step, the effective stiffness of the multilayer lattice is calculated from the effective stiffness of the unit cell obtained in the first homogenization stage. The Voigt³⁸ and Reuss³⁹ models, based on the rule of mixtures, are used to estimate the elastic moduli of the hybrid lattices. For transverse loading conditions (x - or y -direction), the Voigt model applies, assuming uniform strain across all phases. This model computes the effective modulus as a volume-weighted average, as indicated in eqn (10):

$$E_{\text{Voigt}} = \sum_{i=1}^n f_i E_i, \quad (10)$$

where f_i denotes the volume fraction and E_i represents the elastic modulus of the i th phase lattice. Given that the unit cells have equal volume in the three-layer hybrid lattice, f_i equals 1/3. Loading along the x - and y -directions satisfies the assumptions of the Voigt model, which yields an upper bound on the effective modulus as the phases deform in parallel. In contrast, longitudinal loading along the z -direction follows the Reuss model, which assumes uniform stress across all phases and yields the inverse-volume-weighted

modulus presented in eqn (11).

$$E_{\text{Reuss}} = \left(\sum_{i=1}^n \frac{f_i}{E_i} \right)^{-1}. \quad (11)$$

This model yields the lower bound of the effective modulus under serial load sharing, relevant to z-axis loading in this study. Altogether, these models provide a reference for interpreting simulation results and assessing relative stiffness and anisotropy in the lattice configurations.

3. Results and discussion

This study quantitatively evaluates the EM response and mechanical stiffness of single-layer and multilayer configurations composed of SC, BC, and OT lattices. The reliability of the EM simulation is validated by comparing the numerically obtained absorption spectrum with experimental data reported in previous studies.^{24,26} As shown in Fig. S2, the simulated and experimental results show reasonable agreement across the broadband frequency range, demonstrating that the FEM-based model captures the EM response of the CB-PLA lattice absorbers.

3.1. Multilayer lattice structures as EMAs

Fig. 3 compares the EM absorption performance of single-layer SC, BC, and OT lattices (30-mm-thick) and multilayer SC, BC, and OT lattices composed of three 10 mm layers across the 4–18 GHz band. Relative densities (ρ/ρ_s) of 0.1, 0.2, and 0.3 are applied to each unit cell. Solid lines denote single-layer results, while dashed lines represent vertically stacked multilayer results. Single-layer lattices exhibit pronounced absorption peaks at discrete frequencies, whereas multilayer lattices demonstrate relatively stable broadband absorption. For instance, SC and BC single-layer structures exhibit common absorption peaks near 8 GHz and 15 GHz. Notably, multilayer structures dissipate residual EM energy through multiple internal reflections and scattering. Consequently, they achieve more uniform absorption across the frequency range. Multilayer BC and OT lattices maintain an average absorption above 0.9 at a volume fraction of 0.1, indicating stable broadband absorption performance.

To further validate these simulation results and provide physical insight into the observed trends, the effective medium theory (EMT) model is employed for comparison. For reference, the response of the homogenization model predicted by EMT is plotted as a gray dotted line. Here, we apply a linear approximation to estimate the effective permittivity (ϵ_{eff}) of porous

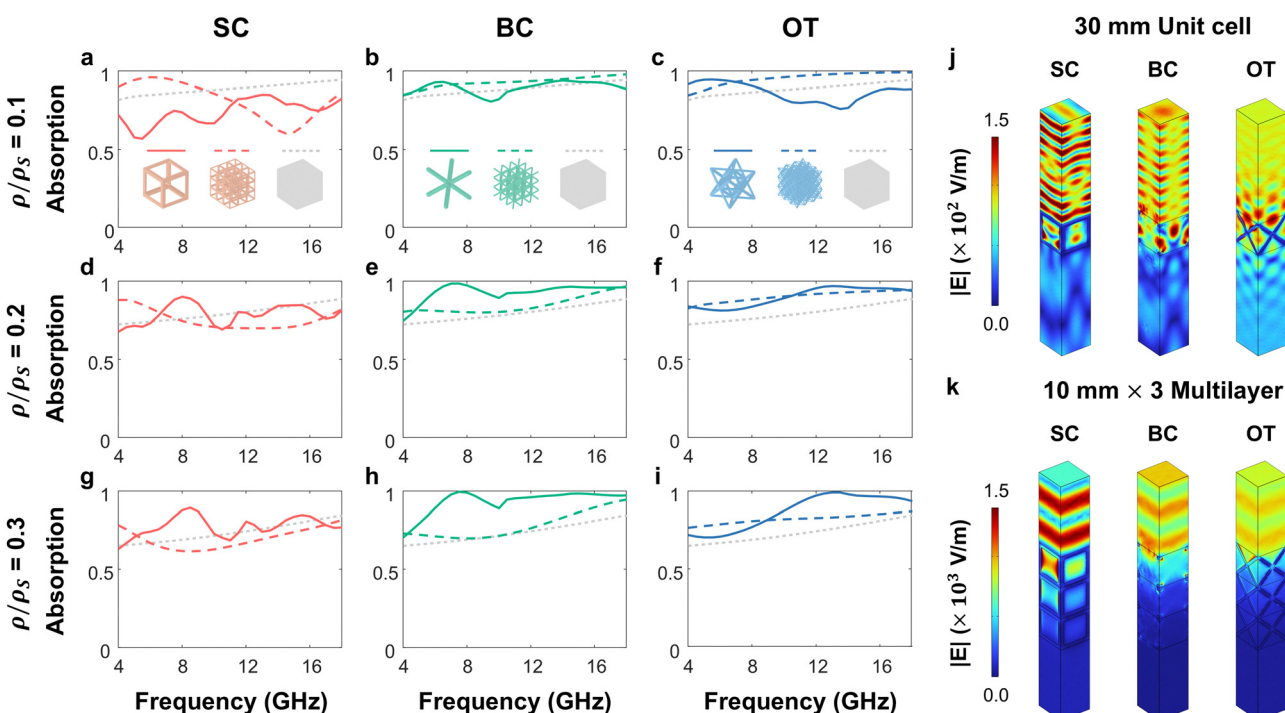


Fig. 3 EM absorption performance of single-layer and multilayer lattice structures composed of three lattice types (SC, BC, and OT) evaluated at various relative volume fractions. (a)–(i) Absorption spectra from 4 to 18 GHz for single-layer structures (solid lines) and three-layer multilayer structures (dashed lines) at relative densities of 0.1, 0.2, and 0.3. Each column corresponds to a specific lattice type: SC (red), BC (green), and OT (blue). For reference, the response predicted by effective medium theory is plotted as a gray dotted line. Multilayer configurations exhibit broader and more uniform absorption compared to their single-layer counterparts, especially at lower densities. (j) and (k) Electric field distributions at 14 GHz for structures with a relative density of 0.1. The single-layer structure (j) permits greater EM wave transmission than the multilayer structure (k), as indicated by the higher electric field intensity observed in the air region beneath the structure.

composites, as indicated in eqn (12), which incorporates porosity (α) as a structural parameter. The corresponding effective impedance (Z_{eff}), derived from eqn (13), provides a simplified means of predicting EM behavior based on geometric and material parameters.^{40,41}

$$\epsilon_{\text{eff}} = \alpha\epsilon_{\text{CB-PLA}} + (1 - \alpha)\epsilon_{\text{air}} \quad (12)$$

$$Z_{\text{eff}} = \sqrt{\frac{\mu_{\text{eff}}}{\epsilon_{\text{eff}}}} \quad (13)$$

In the above equations, $Z_0 \approx 377 \Omega$ denotes the impedance of free space. Under low volume fraction conditions, increased porosity reduces both ϵ_{eff} and μ_{eff} , thereby enhancing impedance matching. This effect accounts for the high average absorption (≥ 0.9) observed in BC and OT lattices at a volume fraction of 0.1. Specifically, it minimizes reflection at the surface while allowing energy to enter and be absorbed within the internal lattice structure.

We find that stacking does not uniformly enhance broadband absorption. In SC lattices, distinct resonance peaks appear at 8, 12, and 16 GHz owing to their structural connectivity (Fig. 3(a), (d) and (g)). BC lattices exhibit similar resonance profiles across all densities, with peaks near 8 GHz persisting in single-layer configurations. At volume fractions of 0.2 or higher, multilayer stacking yields limited additional benefit (Fig. 3(e) and (h)). In contrast, OT lattices display the most notable improvement at low density. At a volume fraction of 0.1, average absorption increases from 0.86 to 0.95 when the lattice is configured as a multilayer structure (Fig. 3(c)). As the volume fraction increases, the peaks and troughs at 8 and 12 GHz intensify (Fig. 3(f) and (i)).

Fig. 3(j) and (k) depict the electric field distributions for single-layer and multilayer SC and OT lattices at a volume fraction of 0.1 and a frequency of 14 GHz. Single-layer structures (Fig. 3(j)) retain a strong residual electric field at the bottom surface, indicating partial wave transmission. In SC lattices, the field concentrates more strongly near the top surface than in OT lattices, suggesting that internal reflections and interference are more pronounced near the top of the SC structure. When the incident EM wave reaches the lattice surface, the degree of impedance matching with free space determines how effectively the energy enters the structure. Proper impedance matching minimizes reflection and allows most of the wave to enter the lattice, initiating internal propagation. As the wave travels through the periodic struts, part of the energy is reflected and scattered, while the rest penetrates deeper into the structure. This process creates localized electric fields at specific junctions, marking regions of strong energy coupling and efficient absorption.

EM wave absorption in multilayer lattice absorbers depends on the interaction between geometry and the incident wavelength. This study considers three primary loss mechanisms. Quarter-wavelength resonance occurs when the absorber thickness is one quarter of the incident wavelength, producing strong low-frequency attenuation through destructive interference between the incident wave and the wave reflected from the

rear surface.⁴² Because the current design lacks a perfect electric conductor (PEC) backing at the bottom surface, its absorption is lower than that of a PEC-backed structure. In practical absorber applications, a PEC or metallic backing is commonly incorporated to suppress transmission and enhance absorption. Introducing a PEC layer effectively blocks transmission and increases internal energy dissipation through reflection, thereby improving overall absorption performance. As shown in Fig. S3, adding a PEC layer readily achieves broadband average absorption exceeding 90% for both BC- and OT-based absorbers. In this study, however, the PEC backing is intentionally excluded to isolate the intrinsic structural contribution of the lattice itself to EM absorption, ensuring that the observed behavior originates solely from the geometric impedance characteristics of the lattice rather than from metallic reflection.

Structural resonance, induced by geometry-dependent multiple reflections at layer interfaces or between adjacent unit cells in the multilayer stack, gives rise to multiple absorption peaks in the mid-frequency range.^{43,44} For example, distinct peaks near 8 GHz are evident in the single-layer spectra depicted in Fig. 3(d), (e), (g) and (h), and the BC lattice exhibits an intrinsic resonant mode that persists across volume fractions.

At higher frequencies, edge diffraction governs the absorption response. Sharp strut edges, pores, and corners scatter the incident field, and this scattering intensifies at the upper and intermediate interfaces of multilayer assemblies, thereby enhancing high-frequency absorption.^{45,46} To activate these mechanisms and achieve broadband performance, geometric parameters, such as strut length, cell spacing, and layer thickness, must remain proportionate with the incident wavelength. The intricate lattice architecture in the optimized topology facilitates the excitation of multiple resonant modes, which contributes to broadband EM absorption. In contrast, simpler geometries such as the SC lattice offer fewer resonance pathways and shorter internal reflection paths, thereby limiting their effectiveness.

Overall, multilayer lattice stacks enhance average absorption and stabilize broadband EM response, making them well-suited for practical absorber applications. Among the three lattices examined, the OT geometry consistently delivers reliable absorption and robust broadband performance in both single-layer and stacked configurations, reinforcing its selection as the preferred top-layer component in multilayer absorbers.

3.2. EM response of hybrid multilayer structures

To clarify the absorption mechanisms of hybrid lattices, EM responses—absorption, reflection, and transmission—are systematically evaluated across the 4–18 GHz band. The obtained results are further supported by spatial distributions of electric field, magnetic field, and power loss. Fig. 4(a–l) depicts the computed responses for both single-layer and multilayer configurations of SC, BC, and OT lattices. The topmost layer is used as the structural reference. In BC- and OT-based multilayer

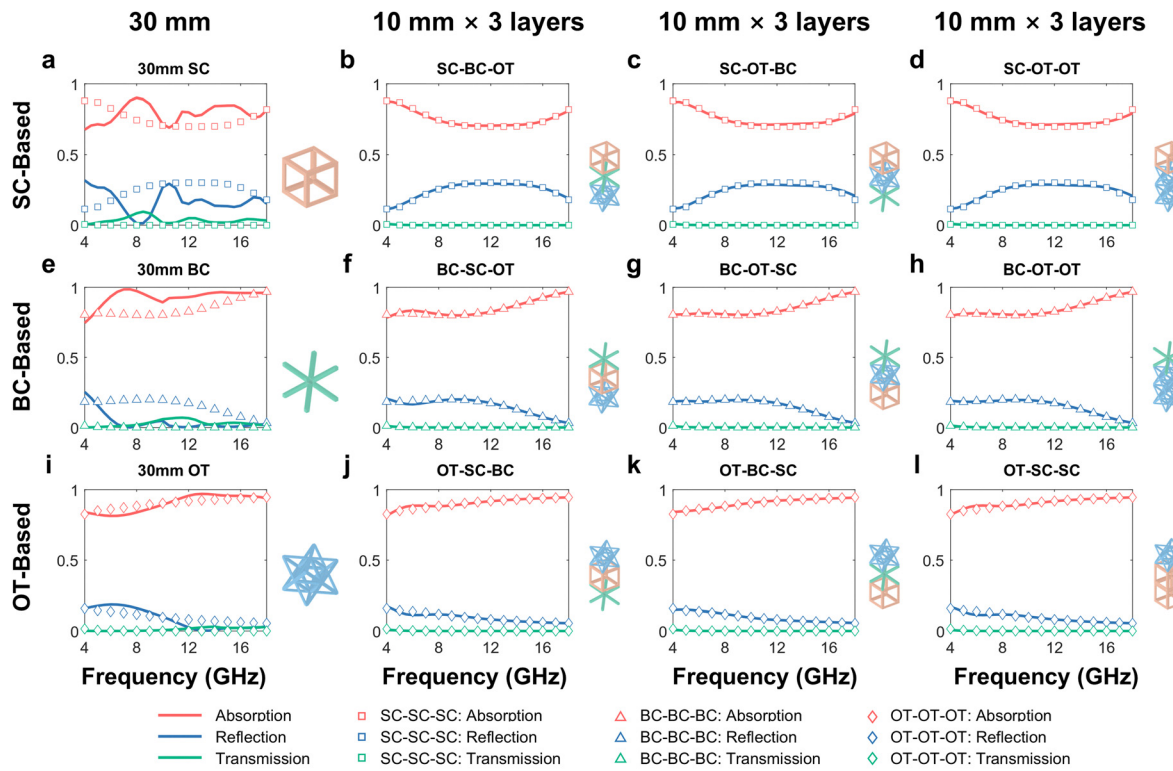


Fig. 4 EM response of single-layer and multilayer lattice structures under normal incidence. (a)–(l) Absorption, reflection, and transmission spectra over the 4–18 GHz frequency range for structures with a relative density of 0.1. Each row corresponds to a different stacking sequence based on SC (a)–(d), BC (e)–(h), and OT (i)–(l) lattices. Solid, dashed, and dotted lines represent absorption, reflection, and transmission, respectively. Multilayer configurations with OT positioned in the top layer (e.g., OT-SC-SC and OT-BC-SC) exhibit broader absorption bandwidth and lower reflection than their single-layer counterparts. (m) and (n) Electric (m) and magnetic (n) field distributions at 5 GHz and 15 GHz for OT-OT-OT and OT-SC-SC multilayer structures. The OT-SC-SC configuration displays stronger field confinement, particularly at higher frequencies. (o) Power-loss distributions corresponding to the same structures and frequencies.

structures (Fig. 4(f–h) and (j–l)), the average absorption exceeds 0.9 across the entire band. Configurations featuring an OT top layer exhibit reduced reflection, indicating that EM behavior is primarily governed by the properties of the uppermost phase.

The transmission response (Fig. 4(a–l)) further illustrates that multilayer configurations attenuate EM waves more effectively than single-layer designs, as evidenced by the reduced field penetration into the lower layers. Fig. 4(m) and (n) corroborate this result, indicating that over 90% of the incident energy is dissipated within the upper layers. The small fraction that passes through the top layer continues to propagate and is gradually absorbed in the subsequent layers.

The E-field and H-field distributions of the OT-SC-SC (Fig. 4(m)) and OT-OT-OT (Fig. 4(n)) configurations, evaluated across different frequencies, reveal a persistent concentration of EM fields within the top OT layer. This pattern supports the earlier finding that the EM characteristics of the uppermost layer predominantly dictate the overall response. At higher frequencies (*e.g.*, 15 GHz), both electric and magnetic fields remain confined near the surface, while at lower frequencies (*e.g.*, 5 GHz), they extend deeper into the multilayer stack. This trend aligns with established EM wave propagation principles, wherein shorter wavelengths induce stronger reflection and diffraction at structural interfaces, resulting in shallower penetration.

Fig. 4(o) shows the spatial distribution of power loss within the lattice. This stage represents how the transmitted EM wave penetrates through the porous network, where its energy is gradually transformed into heat *via* dielectric, conduction, and magnetic losses. Accordingly, the power loss distribution indirectly visualizes the energy transport pathways inside the lattice. In both configurations, power loss is the highest in the

uppermost layer, while the remaining energy dissipates progressively through internal reflections and multiple scattering. The power loss distributions in the top layers of the OT-OT-OT and OT-SC-SC configurations (Fig. 4(o)) display nearly identical localization patterns, consistent with their comparable broadband absorption performance. In the OT lattice, power loss extends along continuous transmission paths through the struts, demonstrating that geometric features govern where field concentration and energy dissipation occur. In the SC lattice, limited penetration confines power loss near the top layer and enhances near-surface interference.

These findings demonstrate that achieving lightweight multilayer absorbers with reliable EM absorption performance requires more than the mere addition of layers. Optimal performance relies on the coordinated design of the top layer geometry, interlayer stacking order, and microstructural features. This study underscores the critical role of layer arrangement in shaping the overall EM response.

3.3. Effect of the incident angle on the EM response of OT-based multilayer structures

The angular stability of EM absorption in OT-based multilayer lattices is assessed by measuring absorptivity at incidence angles from 0° to 75° for both transverse electric (TE) and transverse magnetic (TM) polarizations, as depicted in Fig. 5. All three configurations (single layer OT, OT-OT-OT, and OT-SC-SC) exhibit a gradual decline in absorption with increasing incidence angle. At normal incidence (0°), the structures display nearly identical TE and TM responses (red curves), a result of the rotational symmetry of the OT lattice. This symmetry ensures that EM waves follow equivalent propagation paths regardless of polarization, leading to identical resonance behavior.

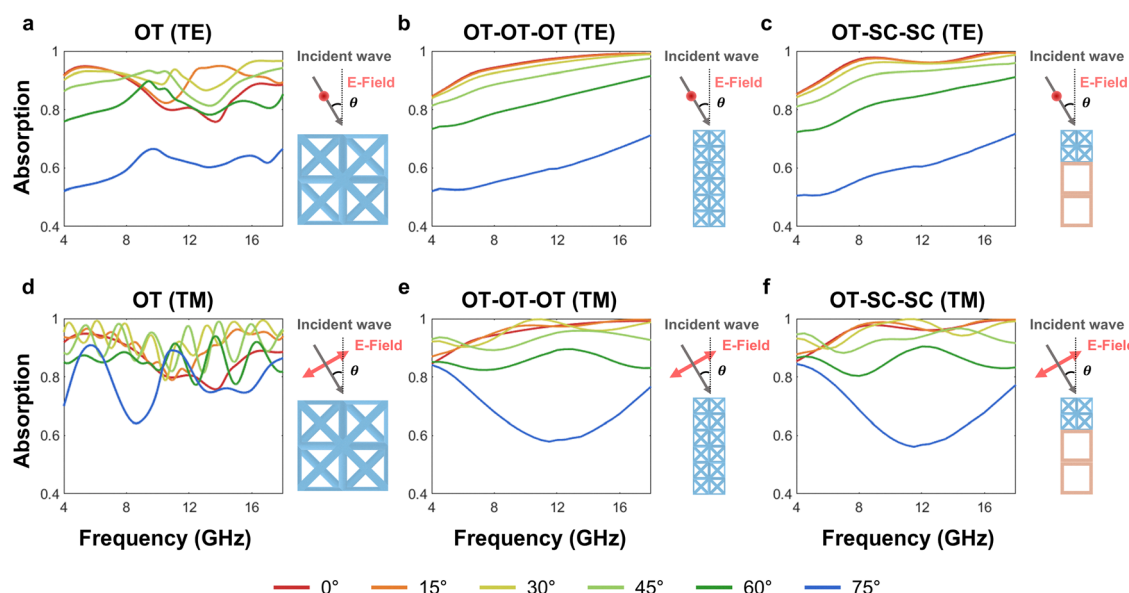


Fig. 5 Comparative analysis of EM wave absorption in 30-mm-thick OT, OT-OT-OT, and OT-SC-SC lattice structures under varying incident angles and polarizations. Panels (a)–(c) illustrate the absorption performance under TE polarization, while panels (d)–(f) depict the results under TM polarization. Each plot presents angle-dependent absorption over the 4–18 GHz frequency range for incident angles of 0°, 15°, 30°, 45°, 60°, and 75°.

As the angle of incidence increases, the TE and TM responses begin to diverge. The absorption spectrum of the single-layer OT structure changes substantially with the angle, and the resonance peak positions shift across the band (Fig. 5(a) and (d)). Under TE polarization, absorption decreases overall, accompanied by a downward shift in the peaks. In contrast, TM polarization results in enhanced absorption in specific frequency ranges and shifts to different peak positions, indicating distinct polarization-dependent characteristics at oblique angles. Although TM-polarized absorption generally decreases with increasing incident angle, certain frequency bands exhibit elevated absorptivity. At 30° incidence, absorptivity increases notably in the 10–12 GHz range. The oblique incidence directs waves along longer internal paths, intensifying interference and thereby enhancing absorption. TM polarization includes a vertical electric field component that promotes additional energy dissipation around vertical struts and interlayer nodes. Consequently, power loss becomes more localized at these frequencies, as illustrated in Fig. 6.

Fig. 6 presents spatial power loss distributions for the overall structure, top layer, and middle layer at 13 GHz and 45° incidence under both TE and TM polarizations. These distributions reveal distinct differences in absorption mechanisms between the OT-OT-OT and OT-SC-SC configurations. In both structures, power loss is concentrated primarily in the top layer, confirming that the incident wave is mainly absorbed by the first layer it encounters. Under identical angular and frequency conditions, the OT-SC-SC structure exhibits approximately 2% lower overall absorptivity than the OT-OT-OT configuration (Fig. 5(b, c and e, f)), which can be attributed to differences in energy dissipation within the middle layer. In the multilayer configuration, this process continues sequentially across layers. The wave transmitted from the top layer enters the middle layer, following different strut orientations where multiple reflections and scattering redirect the residual EM energy. Along these transmission paths, the remaining energy is

redistributed and gradually dissipated through internal losses, leading to cumulative absorption across layers and contributing to the broadband response observed in the OT-OT-OT structure.

In the OT-OT-OT configuration, the wave transmitted from the top layer propagates through the middle OT layer and is absorbed in a relatively uniform manner (e.g., Fig. 6). Under TE polarization, regions of concentrated power loss in the middle layer correspond to those in the top layer, indicating repeated absorption at structurally resonant sites. Under TM polarization, power loss in the middle layer is more evenly distributed along the struts compared to the top layer. This distribution likely results from diagonal strut arrangements that promote internal scattering and multiple reflections, thereby suggesting more effective energy dispersion under TM incidence.

In contrast, the OT-SC-SC configuration displays a more localized power loss distribution within the SC middle layer, with dissipation concentrated at discrete sites. This localization leads to a modest reduction in overall absorption efficiency. The observed disparity in absorptivity between the two configurations highlights the importance of middle-layer lattice geometry and EM properties in governing energy distribution and absorption behavior. These findings suggest that multilayer designs must consider both the geometric characteristics of each layer and the wavelength-matching conditions across the stack. Although the SC lattice absorbs less EM energy, it offers superior mechanical stiffness, making it a favorable reinforcement layer for balancing EM and structural performance. In this study, the OT-SC-SC structure demonstrates broadband absorption comparable to that of OT-OT-OT, even under oblique incidence, affirming its suitability for applications requiring broad-angle performance.

3.4. Mechanical stiffness of multilayer structures

Although strong EM absorption is essential for the functionality of metamaterial absorbers, insufficient mechanical stiffness

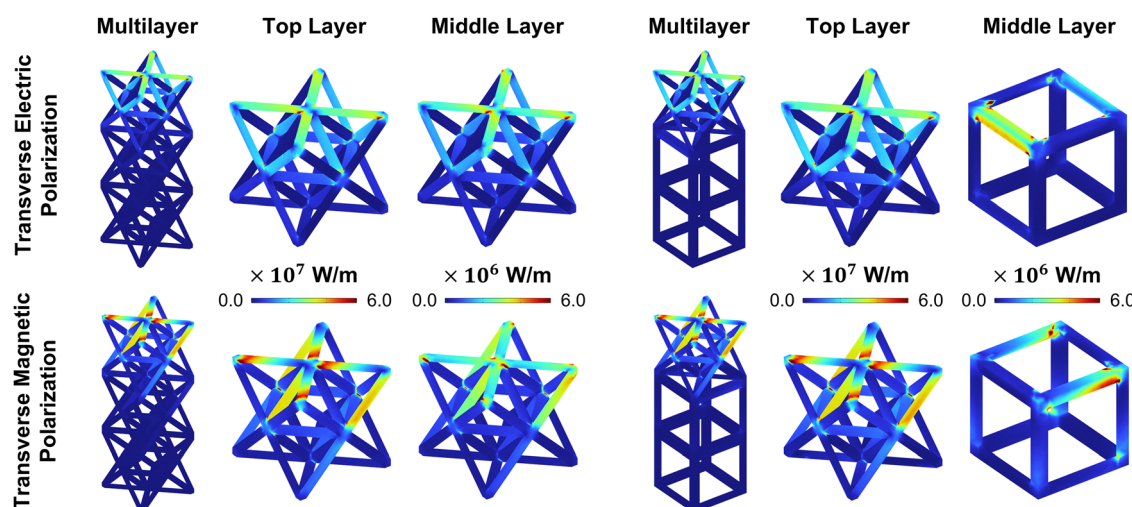


Fig. 6 Power-loss distributions in OT-OT-OT and OT-SC-SC multilayer lattice structures at 13 GHz under 45° oblique incidence, evaluated for both TE and TM polarizations. The visualizations depict the complete three-layer structures alongside the individual top and middle lattice layers.

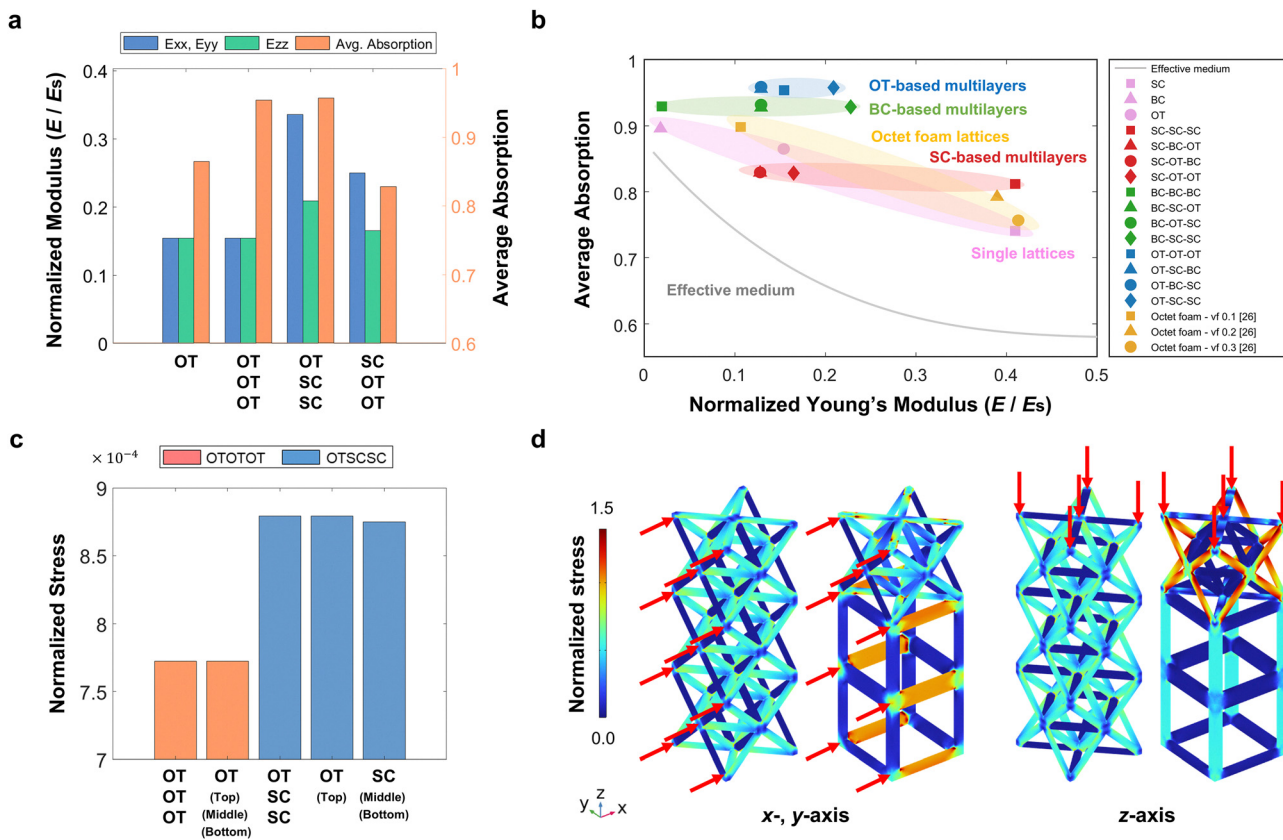


Fig. 7 Comparison of mechanical stiffness and EM wave absorption in single-layer and multilayer lattice structures. (a) Relative Young's modulus and average absorption (4–18 GHz) for OT, OT-OT-OT, OT-SC-SC, and SC-OT-OT. Blue bars represent modulus in the x- and y-directions, while green bars indicate modulus in the z-direction. OT-SC-SC achieves the highest stiffness and maintains strong EM absorption, demonstrating balanced mechanical and EM performance. (b) Absorption-normalized Young's modulus for the selected configurations. The gray line denotes the effective medium approximation. Data categories include single-layer structures (pink), SC-based multilayers (red), BC-based multilayers (green), OT-based multilayers (blue), and octet-foam structures²⁴ (yellow). (c) Layer-specific normalized stress distributions in OT-OT-OT and OT-SC-SC under 1% compressive strain. OT-SC-SC exhibits higher average stress. (d) von Mises stress distributions for OT-OT-OT and OT-SC-SC under 1% compressive loading along the x-, y-, and z-axes.

can substantially limit their practical applicability. To address this limitation, the present study quantitatively evaluates the relative mechanical stiffness of various lattice configurations and combinations. It also investigates whether balanced design strategies can simultaneously optimize EM wave absorption and structural stiffness.

Fig. 7(a) compares the relative modulus and average absorption of four configurations across the 4–18 GHz range: single-layer OT, OT-OT-OT, OT-SC-SC, and SC-OT-OT. The OT-OT-OT structure maintains the same stiffness as the single-layer OT while improving average absorption by 10.35%. OT-SC-SC achieves an average absorption of 95.75%, nearly matching that of OT-OT-OT (95.44%). OT-SC-SC enhances the relative modulus along the z-direction by 36.6% compared to OT-OT-OT, with even greater improvements of up to 118% in the x- and y-directions. In contrast, SC-OT-OT, which incorporates an SC top layer, yields only a 7.4% increase in stiffness, while its average absorption drops to 82.92%. These findings indicate that an OT top layer reliably sustains high absorption levels (> 95%), whereas introducing an SC top layer leads to a

marked decline in absorption performance. Because the incident wave initially interacts with the uppermost interface, the impedance of the top layer largely determines the overall EM response. Fig. 7(b) expands the scope of this analysis by mapping a wider array of lattice configurations against their absorption-normalized moduli.⁴⁷ Even within this broader design space, OT-SC-SC remains in the leading region, offering the highest modulus for a given level of average absorption.

Fig. 7(c) illustrates the layer-resolved stress fields under 1% uniaxial compression, providing insight into the stiffness increase of the OT-SC-SC lattice. Under the same loading conditions, OT-OT-OT sustains stresses identical to those in a single OT layer, whereas the volume-averaged stress in OT-SC-SC exceeds that of OT-OT-OT by 13.8%. Fig. 7(d) presents the von Mises stress distributions for the OT-OT-OT and OT-SC-SC lattices under 1% compressive strain applied along the x, y, and z directions. Because the responses along the x and y directions are symmetric, only the x-direction result is displayed for lateral loading. Under identical deformation, the OT-SC-SC lattice bears higher average stress, confirming its greater modulus.

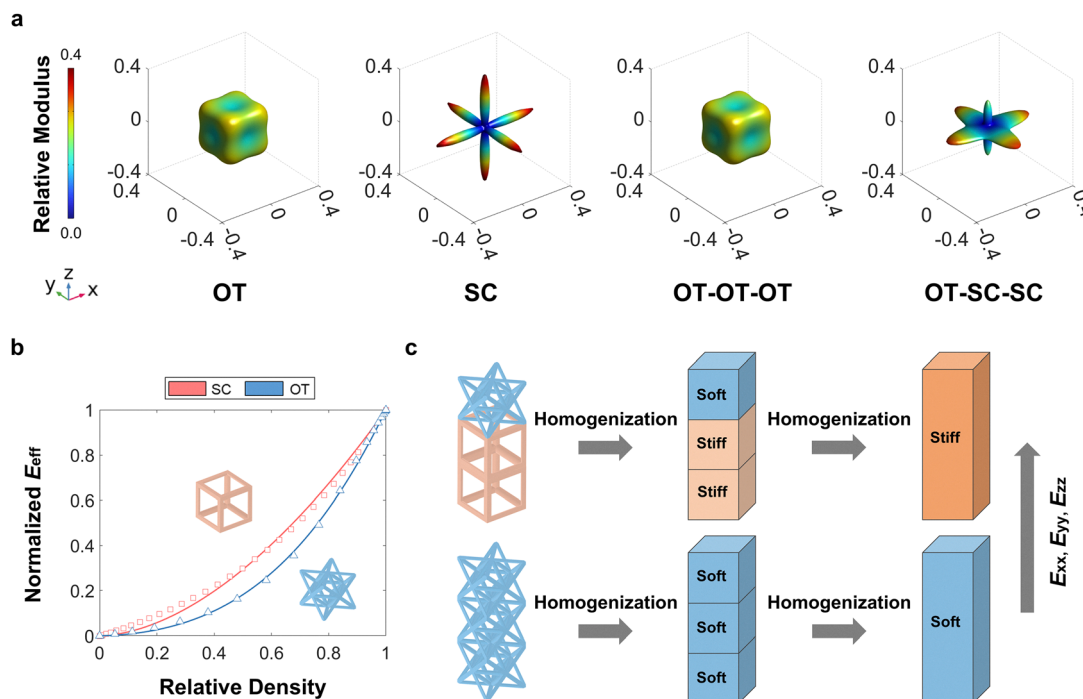


Fig. 8 Comparison of directional modulus distributions, density-dependent stiffness behavior, and homogenization-based optimization strategies for various lattice configurations. (a) Three-dimensional modulus surface plots depicting the directional effective elastic modulus for single-layer OT, multilayer OT–OT–OT, and multilayer OT–SC–SC structures. (b) FEA predictions of relative elastic modulus as a function of relative density (ρ/ρ_0) for SC and OT unit cells. (c) Schematic illustration of a homogenization-guided strategy for mechanical optimization. Strategically layering stiff (SC) and compliant (OT) lattices enables simultaneous enhancement of mechanical stiffness and EM absorption.

Fig. 8(a) clearly illustrates the anisotropic mechanical response of different configurations. Each plot depicts the directional Young's modulus of the lattice as a color-coded surface in three-dimensional space. At each point, the color and radial distance from the origin together indicate the elastic modulus in that direction, normalized by the modulus of the base material. The single-layer OT and OT-OT-OT structures exhibit a relative modulus variation of $(E_{\text{max}} - E_{\text{min}})/E_0 = 0.1079$, resulting in nearly spherical modulus surfaces and indicating an isotropic response with minimal directional variation. In contrast, the OT-SC-SC configuration displays an elongated ellipsoidal modulus surface, with pronounced maxima of 0.3364 along the x- and y-directions and 0.2066 along the z-direction. This anisotropic pattern results from the stretching-dominated SC lattice, which enhances axial stiffness when placed in the lower layers.

For the OT-SC-SC lattice, the modulus variation increases to 0.2901, reflecting considerably higher anisotropy owing to the influence of the SC phase. When the SC lattice is positioned in the bottom layer, it markedly increases overall stiffness according to the Voigt model, thereby enhancing the x- and y-direction stiffness. In contrast, stiffness along the z-direction remains limited because the layers transfer stress in series, as described by the Reuss model. The SC lattice's strong intrinsic anisotropy ($E_{\text{max}}/E_0 = 0.4901$, $E_{\text{min}}/E_0 = 0.0294$) thus governs the overall mechanical response of the OT-SC-SC configuration.

Each unit-cell layer in the three-layer structures has distinct mechanical properties, leading to direction-dependent effective

stiffness. Under compressive loading along the z-axis, the layers act in series and carry the same stress. This behavior follows the Reuss model, wherein the overall stiffness is governed by the weakest layer and approaches the lower bound. In contrast, along the x- and y-directions, the layers are arranged in parallel and experience the same strain. This loading behavior corresponds to the Voigt model. In this configuration, the stiffer SC layers dominate the mechanical response, driving the stiffness toward the Voigt upper bound. The relative modulus increases from 0.154 in OT-OT-OT to 0.336 in OT-SC-SC, representing a gain of 118%. OT-SC-SC exhibits considerably higher stiffness and emerges as a promising candidate for absorber designs requiring both mechanical integrity and EM performance.

Fig. 8(b) illustrates that the OT and SC unit cells exhibit distinct deformation mechanisms due to differences in their beam geometries. Across the full range of relative densities, the SC lattice consistently achieves a higher normalized modulus than the OT lattice. These results demonstrate that strategically combining layers with contrasting mechanical properties enables multilayer designs such as OT-SC-SC to achieve superior overall stiffness relative to OT-OT-OT configurations.

Placing the OT lattice in the top layer and the SC lattice in the bottom layer offers an effective strategy for simultaneously optimizing EM absorption and mechanical reinforcement. The upper OT layer facilitates efficient absorption of incident waves, whereas the underlying SC layer enhances structural stiffness, as depicted in Fig. 8(c). While previous studies have reported that improving mechanical rigidity often leads to reduced EM

Published on 03 December 2025. Downloaded by Ewha Womans University on 12/15/2025 9:56:24 PM.

performance due to decreased internal scattering and impedance mismatch,⁴⁸ the proposed hybrid configuration successfully mitigates this trade-off. Maintaining high mechanical stiffness is crucial for ensuring structural integrity and maintaining EM performance under operational stresses such as mechanical loading and vibration, which are common in real-world environments. This layer-specific approach provides a practical framework for designing multifunctional metamaterial systems that integrate EM functionality with mechanical stiffness. Such designs are particularly advantageous for lightweight platforms such as drones and aircraft that require both load-bearing capability and EMI shielding.

4. Conclusion

This study presents the design and systematic evaluation of multilayer lattice structures to elucidate the relationship between EM wave absorption and mechanical stiffness. It investigates OT, BC, and SC lattices in both single-layer and multilayer configurations to analyze how each structural arrangement influences EM performance and mechanical response. From an EM perspective, the OT lattice consistently exhibits strong broadband absorption over the 4–18 GHz frequency range in both single-layer and multilayer configurations. When placed in the top layer of a multilayer assembly, the OT lattice facilitates impedance matching with incident waves and markedly reduces reflection. In contrast, the SC lattice exhibits weaker absorption but provides superior mechanical stiffness owing to its high relative modulus. Compared to single-layer designs, multilayer structures exhibit more stable broadband absorption. The OT-SC-SC configuration, for example, maintains average absorption above 95% over the 4–18 GHz range, which is similar to the OT-OT-OT structure, while achieving a 36.6% increase in stiffness along the z-direction and a 118% increase along the x- and y-directions. Simulation results suggest that placing the OT layer at the top improves impedance matching with the surrounding medium and contributes to high absorption. Adding an SC layer at the bottom further enhances overall stiffness.

Mechanical analysis indicates that inserting stiff SC layers into the stack increases the overall load-bearing capacity. The OT-SC-SC assembly achieves a 36.6% higher z-direction effective elastic modulus and 118% higher x- and y-direction effective elastic moduli than the OT-OT-OT configuration while maintaining an average absorption of above 95%. This design, thus, demonstrates that mechanical reinforcement can be achieved without sacrificing EM performance.

Overall, our results confirm that strategically combining different lattice geometries within multilayer structures enables balanced optimization of EM and mechanical properties. Positioning the OT lattice at the top for superior EM wave absorption and the SC lattice at the bottom for mechanical reinforcement represents an effective design strategy. Overall, the proposed design framework offers guidance for developing multifunctional metamaterials and is applicable to domains

such as EMI shielding, EM protection systems, and lightweight structural armor.

Author contributions

Hyoui Yoon: writing – review and editing, writing – original draft, visualization, software, methodology, investigation, formal analysis, data curation; Dahyun Daniel Lim: writing – review and editing, writing – original draft, software, investigation, formal analysis; Grace X. Gu: writing – review and editing, writing – original draft, supervision, methodology, conceptualization; Sangryun Lee: writing – review and editing, writing – original draft, supervision, project administration, methodology, funding acquisition, conceptualization.

Conflicts of interest

There are no conflicts to declare.

Data availability

The data supporting this article have been included as part of the supplementary information (SI). Supplementary information is available. See DOI: <https://doi.org/10.1039/d5mh01846c>.

Acknowledgements

H. Y. and S. L. acknowledge support by the National Research Foundation of Korea (NRF) grant funded by the Korean government (MSIT) (RS-2025-24803153). D. L. and G. G. acknowledge support by the Office of Naval Research (N00014-25-1-2534) and Alfred P. Sloan Foundation.

References

- 1 B. X. Wang, C. Xu, G. Duan, W. Xu and F. Pi, *Adv. Funct. Mater.*, 2023, **33**, 2213818.
- 2 E. Wen, X. Yang and D. F. Sievenpiper, *Nat. Commun.*, 2023, **14**, 7736.
- 3 J. You, Q. Ma, L. Zhang, C. Liu, J. Zhang, S. Liu and T. Cui, *Electromagn. Sci.*, 2023, **1**, 1–33.
- 4 M. F. Elmahaishi, R. a S. Azis, I. Ismail and F. D. Muhammad, *J. Mater. Res. Technol.*, 2022, **20**, 2188–2220.
- 5 C. Sun, D. Li, T. Liu, Q. An, C. Zhang, Y. Li and W. Liao, *Composites, Part B*, 2024, **280**, 111484.
- 6 H. Jeong, T. T. Nguyen and S. Lim, *Sci. Rep.*, 2018, **8**, 17893.
- 7 Q. Huang, G. Wang, M. Zhou, J. Zheng, S. Tang and G. Ji, *J. Mater. Sci. Technol.*, 2022, **108**, 90–101.
- 8 F. Shahzad, M. Alhabeb, C. B. Hatter, B. Anasori, S. Man Hong, C. M. Koo and Y. Gogotsi, *Science*, 2016, **353**, 1137–1140.
- 9 T. Beeharry, R. Yahiaoui, K. Selemani and H. H. Ouslimani, *Sci. Rep.*, 2018, **8**, 382.
- 10 S. H. Kim, S. Y. Lee, Y. Zhang, S. J. Park and J. Gu, *Adv. Sci.*, 2023, **10**, 2303104.

- 11 X. Yan, X. Huang, Y. Chen, Y. Liu, L. Xia, T. Zhang, H. Lin, D. Jia, B. Zhong and G. Wen, *Carbon*, 2021, **174**, 662–672.
- 12 D. D. Lim, J. Lee, J. Park, J. Lee, D. Noh, S. Park, G. X. Gu and W. Choi, *Addit. Manuf.*, 2024, **95**, 104515.
- 13 Q. Zhou, X. Yin, F. Ye, X. Liu, L. Cheng and L. Zhang, *Mater. Des.*, 2017, **123**, 46–53.
- 14 B. Jiang, C. Qi, H. Yang, X. Wu, W. Yang, C. Zhang, S. Li, L. Wang and Y. Li, *Carbon*, 2023, **208**, 390–409.
- 15 F. Zhang, N. Li, J.-F. Shi, L. Xu, L.-C. Jia, Y.-Y. Wang and D.-X. Yan, *Composites, Part B*, 2024, **283**, 111646.
- 16 C. M. Watts, X. Liu and W. J. Padilla, *Adv. Mater.*, 2012, **24**, 98–120.
- 17 X. Chen, H. Liu, D. Hu, H. Liu and W. Ma, *Ceram. Int.*, 2021, **47**, 23749–23761.
- 18 F. Meng, H. Wang, F. Huang, Y. Guo, Z. Wang, D. Hui and Z. Zhou, *Composites, Part B*, 2018, **137**, 260–277.
- 19 Y. Yu, P. Yi, W. Xu, X. Sun, G. Deng, X. Liu, J. Shui and R. Yu, *Nano-Micro Lett.*, 2022, **14**, 77.
- 20 A. Houbi, Z. A. Aldashevich, Y. Atassi, Z. B. Telmanovna, M. Saule and K. Kubanych, *J. Magn. Magn. Mater.*, 2021, **529**, 167839.
- 21 D. S. Aherrao, C. Singh and A. Srivastava, *J. Appl. Phys.*, 2022, **132**, 240701.
- 22 W. Li, J. Wei, W. Wang, D. Hu, Y. Li and J. Guan, *Mater. Des.*, 2016, **110**, 27–34.
- 23 D. Yang, H. Mei, L. Yao, W. Yang, Y. Yao, L. Cheng, L. Zhang and K. G. Dassios, *J. Mater. Chem. C*, 2021, **9**, 12010–12036.
- 24 D. D. Lim, S. Lee, J. H. Lee, W. Choi and G. X. Gu, *Mater. Horiz.*, 2024, **11**, 2506–2516.
- 25 W. Xin, Z. Binzhen, W. Wanjun, W. Junlin and D. Junping, *IEEE Photonics J.*, 2017, **9**, 1–12.
- 26 D. D. Lim, J. Park, J. Lee, D. Noh, J. Lee, J. Choi and W. Choi, *Addit. Manuf.*, 2022, **55**, 102856.
- 27 J. Zhou, T. Koschny, M. Kafesaki and C. M. Soukoulis, *Photonics Nanostructures - Fundam. Appl.*, 2008, **6**, 96–101.
- 28 Q. An, D. Li, W. Liao, T. Liu and W. Li, *Adv. Mater. Technol.*, 2025, e00581.
- 29 C. Ling, A. Cernicchi, M. D. Gilchrist and P. Cardiff, *Mater. Des.*, 2019, **162**, 106–118.
- 30 W. Li, M. Xu, H. X. Xu, X. Wang and W. Huang, *Adv. Mater.*, 2022, **34**, e2202509.
- 31 Q. An, D. Li, W. Liao, T. Liu, Z. Qu, G. Wang and X. Li, *Adv. Funct. Mater.*, 2025, **35**, 2414629.
- 32 E. Maleki, B. Salehnasab, M. Paul, S. Shao and N. Shamsaei, *Mater. Des.*, 2025, 114361.
- 33 M. Abdullahi and M. Ali, *Beni-Suef Univ. J. Basic Appl. Sci.*, 2021, **10**, 24.
- 34 C. Multiphysics, COMSOL Multiphysics, Burlington, MA, accessed Feb, 1998, **9**, 32.
- 35 Q.-Y. Wei, Y.-D. Fang, Z.-B. Sun, Y. Zeng, J. Zhang, J. Lei, L. Xu, H. Lin, G.-J. Zhong and Z.-M. Li, *Composites, Part A*, 2023, **169**, 107516.
- 36 S. Lee, Z. Zhang and G. X. Gu, *Mater. Horiz.*, 2022, **9**, 952–960.
- 37 R. Hill, *J. Mech. Phys. Solids*, 1963, **11**, 357–372.
- 38 W. Voigt, *Ann. Phys.*, 1889, **274**, 573–587.
- 39 A. Reuß, *Z. Angew. Math. Mech.*, 1929, **9**, 49–58.
- 40 L. Yin, J. Doyhamboure, X. Tian and D. Li, *Composites, Part B*, 2018, **132**, 178–187.
- 41 A. Sihvola, *Surf. Sensing Technol. Appl.*, 2000, **1**, 393–415.
- 42 S. Zhang, T. Wang, M. Gao, P. Wang, H. Pang, L. Qiao and F. Li, *J. Phys. D: Appl. Phys.*, 2020, **53**, 265004.
- 43 S. Xie, Z. Ji, Y. Yang, G. Hou and J. Wang, *J. Build. Eng.*, 2016, **7**, 217–223.
- 44 Y. He and R. Gong, *Europhys. Lett.*, 2009, **85**, 58003.
- 45 J. Ning, S. Dong, X. Luo, K. Chen, J. Zhao, T. Jiang and Y. Feng, *Results Phys.*, 2020, **18**, 103320.
- 46 G. L. James, *Geometrical theory of diffraction for electromagnetic waves*, IET, 1986.
- 47 I. Gibson and M. F. Ashby, *Proc. R. Soc. London, Ser. A*, 1982, **382**, 43–59.
- 48 X. Hou, X.-R. Feng, K. Jiang, Y.-C. Zheng, J.-T. Liu and M. Wang, *J. Mater. Sci. Technol.*, 2024, **186**, 256–271.